Hyaluronan (HA), which is the main component of the GAGs, has been shown to improve healing in a variety of tissues through the effects on delivery of growth factors, cellular adhesion and proliferation, and anti-inflammatory reactions [12–15]. These biological effects of HA would also play a crucial role in enhancing ligament tissue regeneration. Alginate is one of the naturally abundant and anionic polysaccharides composed of a disaccharide repeating unit, [GlcAβ(1-4)Glcβ(1-3)]. Moreover, this polysaccharide is known as a hyaluronic acid-like biocompatible polymer often used in biomaterials, because it contains D-glucuronic acid as a main sugar residue of the repeating unit [16, 17]. Chitosan has been employed as an excellent biocompatible material in wound healing and tissue repair [18, 19]. Since it is regarded as a cationic polysaccharide showing excellent cell adhesive properties, hybrid materials composed of chitosan combined with HA or alginate might provide a novel class of polyion complex effective as for ligament and tendon specific scaffold materials.

Tamura *et al.* [20] established a new methodology for preparation of chitosan-coated GAG-mimicking filaments. They also showed enhancement of mechanical strength of the GAG-mimicking filaments by coating chitosan through ionic interaction. To mimic the natural environment of ligament ECM, the present authors have developed novel hybrid-polymer fibres (a chitosan-based HA hybrid-polymer fibre and an alginate-based chitosan hybrid-polymer fibre) as fundamental materials for ligament- and tendon-specific scaffolds. In the present paper, an overview of previous work by the present authors on the development of novel scaffold and tendon tissue engineering is provided. Furthermore, *in-vivo* experiments of biodegradation of the scaffold and ligament reconstruction using tissue engineering technique are studied. All the animal experiments were approved by institutional animal care committees.

2 DEVELOPMENT OF A THREE-DIMENSIONAL SCAFFOLD

Polymer fibres were developed by the wet-spinning method as described by Tamura *et al.* [20] with the modifications described in references [21] and [22]. Briefly, a solution of chitosan oligomer (0, 0.5, or 0.1 per cent w/w; molecular weight, 18 000; Kimitsu Chemical, Co. Ltd, Tokyo, Japan) or sodium alginate (4 per cent w/w; molecular weight, 600 000; Kibun Food Chemifa, Co. Ltd, Tokyo, Japan) was spun into a coagulation system (first coagulation bath, 0.05 or 0.1 per cent HA dissolved in 50 per cent aqueous methanol solution for chitosan–HA hybrid-polymer fibre, or 0.05 or 0.1 per cent chitosan for alginate–chitosan hybrid-polymer fibre; second coagulation bath, 3 per cent $CaCl_2$ in water–methanol) through a nozzle containing 50 holes, each with a diameter of 0.1 mm. HA had a viscosity-averaged molecular weight of 2 400 000 and was donated by Denki Kagaku Kougyo Co. Ltd, Tokyo, Japan (Fig. 1). The fibres were washed with methanol and dried at room temperature and used for the further experiments after sterilization. Sterilization of the three-dimensional scaffold was performed using ethylene oxide gas for 24 h. In the current study, alginate polymer fibre, alginate-based chitosan hybrid-polymer fibres (alginate with 0.05 per cent chitosan, and alginate with 0.1 per cent chitosan), chitosan polymer fibre, and chitosan-based HA hybrid-polymer fibres (chitosan with 0.05 per cent HA, and chitosan with 0.1 per cent HA) were originally prepared. Polymer fibre of Polyglactin 910, a 90 : 10 copolymer of glycolide and lactide, coated with Polyglactin 370 and calcium stearate (9-0 Vicryl suture material, Ethicon Co., Somerville, New Jersey, USA) was also used as a control material. This control material, which has the same diameter as the novel fibres, has been widely used in clinical fields in wound closure.

3 *IN-VITRO* EVALUATION OF SCAFFOLDS FOR LIGAMENT AND TENDON TISSUE ENGINEERING

The material properties of each fibre were measured according to the Japanese Industrial Standard (JIS) L1015 in dry condition (room temperature, 22 ± 2 °C; humidity, 50 per cent). Tensile tests for five samples

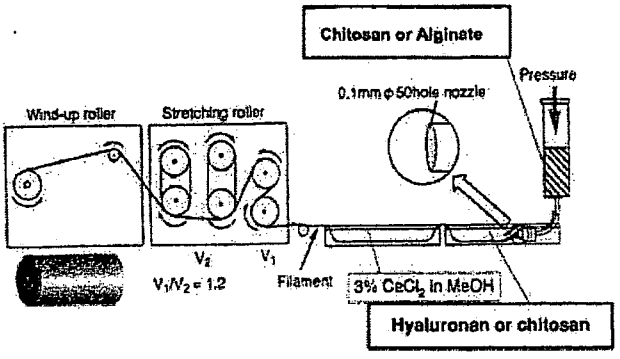

Fig. 1 Schematic diagram of the development of hybrid-polymer fibre scaffolds using the wet-spinning method

of each material were performed at a cross-head speed of 20 mm/min using a materials-testing machine (model P/N346-51299-02, Shimadzu, Kyoto, Japan). The cross-sectional area was determined using an optical microscope (model BX50, Olympus, Tokyo, Japan) and a video dimension analyser (model VM-30, Olympus, Tokyo, Japan). Table 1 summarizes the material properties of each fibre. Hybridization of HA to chitosan fibre increased the tensile strength. On the other hand, hybridization of chitosan to alginate fibre did not increase the tensile strength of the material. The values of all the novel materials were significantly less than those of the control group ($p < 0.0001$). Strain at failure in the control group was significantly higher than those in the chitosan and hybrid groups ($p < 0.0001$).

A cell adhesion study was performed as described in previous reports [**23, 24**]. Briefly, the fibrous samples were cut into 10 mm pieces and tightly packed into polytetrafluoroethylene tubes (30 mm in length, and 7 mm in inner diameter; Sanplatec, Osaka, Japan). Each fibrous sample consisted of 1000 fibres. Then, 0.1 ml of fibroblast suspension from rabbit patellar tendon (1.4×10^7 cells/ml) were loaded on to the column. The cells were allowed to adhere in a humidified incubator for 1 h. Each column was gently rinsed with 1 ml of 1 M phosphate-buffered saline for 30 s using a syringe, and the number of unattached cells was quantified by microscopic observation of the rinsed solution. Five samples in each group were measured. As shown in Fig. 2, HA coating and chitosan coating significantly reduced the number of unattached cells ($p < 0.05$). This effect was more significant in chitosan–HA hybrid fibre. According to these fundamental experiments, it was decided to choose chitosan–0.1 per cent HA hybrid fibre for further study of tendon and ligament scaffolds.

Table 1 Material properties of each fibre in the dry condition

Material	Tensile strength (MPa)	Strain at failure (%)
Control (Polyglactin 910)	440.4 ± 13.8	30.4 ± 02.4
Chitosan	128.1 ± −9.7	4.3 ± 0.8
Chitosan–0.05% HA	152.6 ± 10.8	6.1 ± 1.4
Chitosan–0.1% HA	217.6 ± 16.9	3.2 ± 0.6
Alginate	274.1 ± 4.9	9.0 ± .4
Alginate–0.05 chitosan	221.7 ± .4	10.6 ± .7
Alginate–0.1 chitosan	235.2 ± 8.5	12.3 ± 0.3

$n = 5$ in each sample (mean ± standard deviation).

To test the initial reduction in the strength of the hybrid fibre due to water absorption, the material properties of the chitosan–0.1 per cent HA hybrid fibre were measured after incubation for 0 h, 2 h, 14 days, and 28 days in the standard culture medium (Dulbecco's modified Eagle's medium (D5796; Sigma Chemical Co., St Louis, Missouri, USA)). Five samples were tested in each time period. The tensile strength decreased after incubation for 2 h; however, it was maintained during the period between 2 h and 28 days (Table 2).

Cell proliferation was measured by counting the deoxyribonucleic acid (DNA) content in chitosan, chitosan–0.05 per cent HA, and chitosan–0.1 per cent

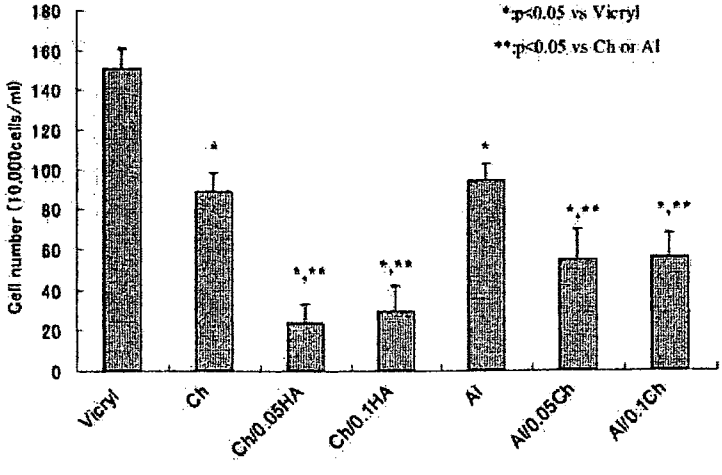

Fig. 2 Number of fibroblasts unattached from control and hybrid-polymer fibres (the data are shown as the mean ± standard deviation ($n = 5$)): Ch, chitosan fibre; Ch/0.05 HA, chitosan-based 0.05 per cent HA hybrid fibre; Ch/0.1HA, chitosan-based 0.1 per cent HA hybrid fibre; Al, alginate fibre; Al/0.05Ch, alginate-based 0.05 per cent chitosan hybrid fibre; Al/0.1Ch, alginate-based 0.1 per cent chitosan hybrid fibre

Table 2 Tensile strength of chitosan–0.1 per cent HA fibre after 0 h, 2 h, 14 days, and 28 days in the standard medium

Incubation time	Tensile strength (MPa)
0 h	213.3 ± 10.0
2 h	60.0 ± 6.7
14 days	66.7 ± 6.8
28 days	65.1 ± 6.6

$n = 5$ in each sample (mean ± standard deviation).

HA hybrid fibre. A 50 μl aliquot of the fibroblast suspension (2.0×10^7 cells/ml) were loaded on to each three-dimensional scaffold. After culture for 1, 7, 14, and 28 days, five of each fibre group were taken for analysis of DNA content to quantify cell proliferation. The DNA content was measured in aliquots of sodium citrate using a modified fluorometric assay with Hoechst dye 33258 (Polysciences Inc, Warrenton, Pennsylvania, USA). The DNA contents (μg/wet weight) were converted using a standard curve of control DNA (043–21751, DNA sodium salt from salmon spermary, Wako Pure Chemical Industries Ltd, Osaka, Japan). Figure 3 shows the DNA contents in chitosan, chitosan–0.05 per cent HA, and chitosan–0.1 per cent HA scaffolds. The DNA contents in the chitosan–0.1 per cent HA scaffold were significantly higher than in other scaffolds after culture for 1 and 28 days.

ECM production of fibroblast from rabbit patellar tendon was observed by light microscopy 14 days after the culture in chitosan–0.1 per cent HA hybrid-polymer fibre scaffolds. Immunostaining for type I collagen was prominent around the chitosan–0.1 per cent HA hybrid fibres after cultivation for 14 days (Fig. 4(a)). Type I collagen was more abundant around the surface of the fibres. On the other hand, type III collagen immunolabelling was not clearly detected around the fibres after cultivation for 14 days (Fig. 4(b)). There was no staining for type II collagen around the fibres.

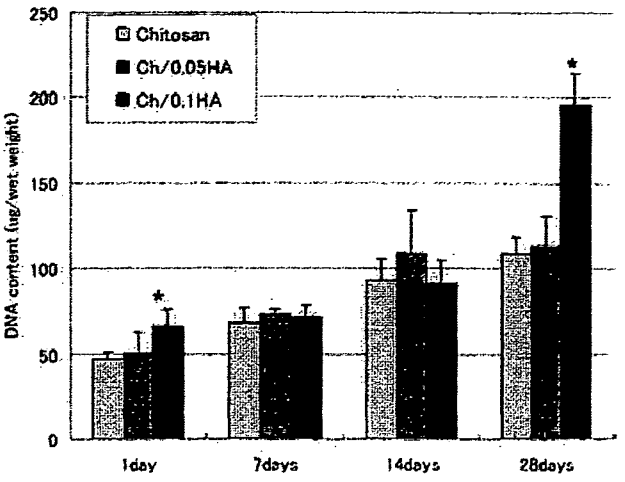

Fig. 3 DNA content in chitosan, chitosan–0.05 per cent HA hybrid fibre, and chitosan/0.1 per cent HA hybrid fibre, where a 50 μl aliquot of the fibroblast suspension (2.0×10^7 cells/ml) was loaded on to each 3D scaffold (the data are shown as the mean ± standard deviation ($n = 5$)): *, $p < 0.05$ versus chitosan and chitosan–0.05 per cent HA

Endotoxin of chitosan was measured using the *Limulus* amoebocyte lysate test with the gel–clot technique (*Limulus* ES-J test, Wako, Osaka, Japan). The amount of endotoxin of chitosan was 0.3 EU/g. This level is the lower limit of sensitivity.

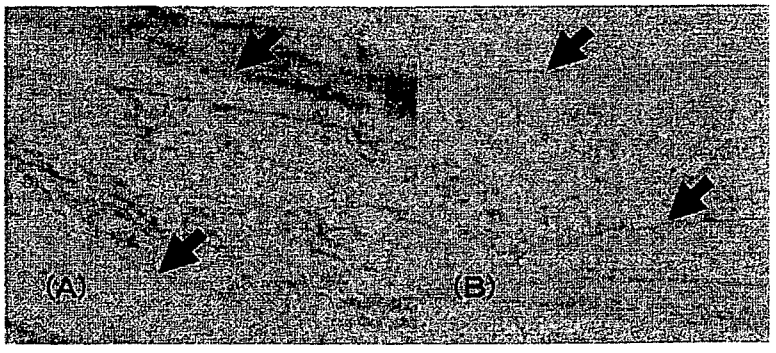

Fig. 4 Immunostaining for (A) type I and (B) type III collagen in chitosan-based 0.1 per cent HA hybrid-polymer fibres after cultivation for 14 days with fibroblasts. The black arrows indicate polymer fibre. Type I collagen was more abundant, and type III collagen was not detected around the fibres (magnification, ×400)

4 *IN-VIVO* EVALUATION OF SCAFFOLDS FOR LIGAMENT AND TENDON TISSUE ENGINEERING

In order to test biodegradation of the chitosan–0.1 per cent HA hybrid fibre, 104 fibres were fabricated (6 mm in width, 80 mm in length, and 1 mm in thickness). Next, 15 fabricated scaffolds were implanted on to the backs of five Wistar-King A (WKA) strain rats. Then, 2, 4, 6, 12, and 16 weeks after implantation, each rat was sacrificed and the maximum failure load of each scaffold was measured. During mechanical testing, samples were carefully kept moist by physiological saline solution. As a control, three scaffolds were mechanically tested in the dry condition (Fig. 5). The maximum failure load was significantly decreased after implantation ($p < 0.05$); 2 weeks after implantation, the maximum failure load was significantly decreased. The failure load was gradually increased thereafter. Finally, 16 weeks after implantation, the load was significantly greater than those after 2 and 4 weeks ($p < 0.05$).

To evaluate the feasibility of tendon tissue engineering using the novel scaffold, rabbit models of rotator cuff tendon defect were created and treated with tissue engineering techniques using chitosan–0.1 per cent HA hybrid polymer fibre scaffold material [25]. Rabbit infraspinatus tendons and their humeral insertions were removed to create defects. Each defect was covered with a fibroblast-seeded scaffold (10 mm in length, 7 mm in width, and 0.7 mm thick) (Fig. 6). A 50 μl aliquot of the fibroblast suspension from rabbit patellar tendon (8.0×10^6 cells/ml) was

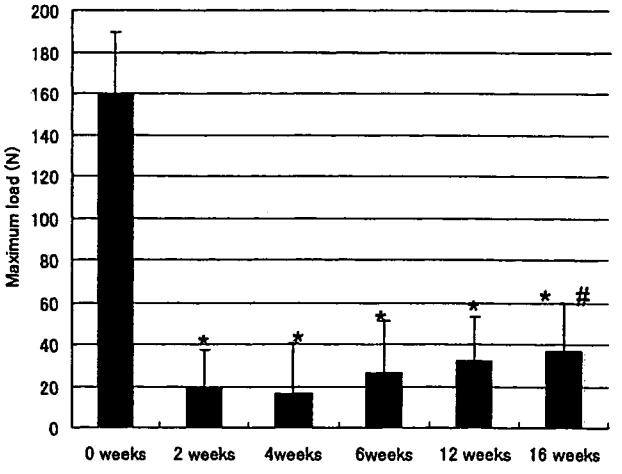

Fig. 5 Maximum failure load of the scaffold implanted in back of five WKA rats (the data are shown as the mean ± standard deviation ($n = 3$)): *, $p < 0.05$ versus 0 weeks; #, $p < 0.05$ versus 2 and 4 weeks

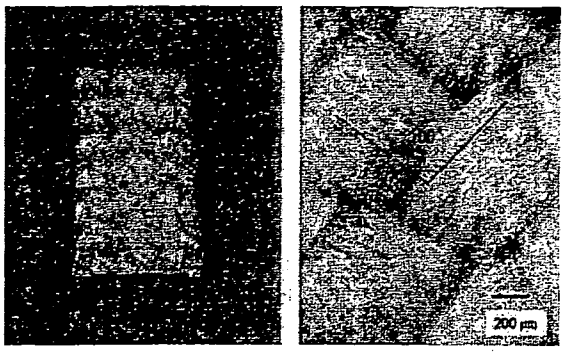

Fig. 6 A three-dimensional scaffold (10 mm in length, 7 mm in width, and 0.7 mm thick) created from 13 braids using a braiding machine

loaded on to each three-dimensional scaffold and cultured for 4 weeks *in vitro* or a non-fibroblast-seeded scaffold. At 4 and 12 weeks after surgery, the rabbits were sacrificed. Engineered tendons were assessed at each time period by histological ($n = 1$), and biomechanical ($n = 5$) analyses. For biomechanical studies, a bone–tendon preparation was mounted and attached to a conventional tensile tester (model P/N346-51299-02, Shimadzu, Kyoto, Japan). The free end of the tendon was secured with a specially designed cryojaw device. During mechanical testing, samples were carefully kept moist by physiological saline solution.

Figure 7 shows a summary of the results of shoulder tendon tissue engineering experiment. Type I collagen was only seen in the fibroblast-seeded scaffold

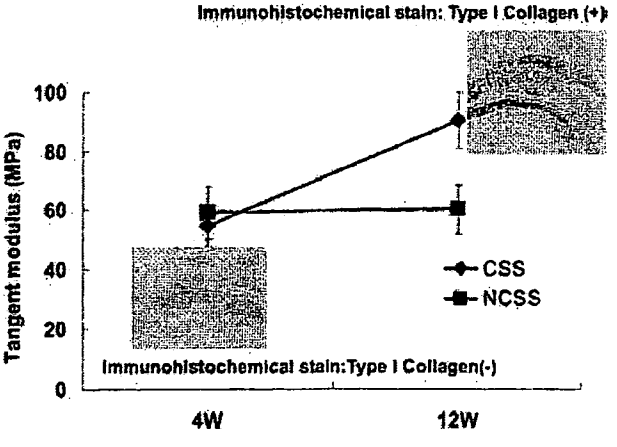

Fig. 7 Summary of rabbit rotator cuff defect models treated with tissue engineering techniques, where the scaffold enhanced the production of type I collagen, and led to improved mechanical strength in the regenerated tissues of the rotator cuff *in vivo* (the data are shown as the mean ± standard deviation ($n = 5$)): CSS, cell-seeded scaffold; NCSS, non-cell-seeded scaffold

and increased in the regenerated tissue with the fibroblast-seeded scaffold. The tensile strength and tangent modulus in the fibroblast-seeded scaffold were significantly improved from 4 to 12 weeks post-operatively. The fibroblast-seeded scaffold had a significantly greater tensile strength and tangent modulus than the non-fibroblast-seeded scaffold at 12 weeks.

For evaluation of ligament tissue engineering, a model of rabbit medial collateral ligament (MCL) injury was used [**26, 27**]. Fibroblasts of Achilles tendon in the same rabbit (1×10^5 cells/mm on the scaffold) were seeded on the chitosan–0.1 per cent HA hybrid-polymer fibre scaffold (40 mm in length, 7 mm in width, and 1 mm in thickness), and cultured for 2 weeks. MCL was removed and reconstructed using the engineered scaffold through bone tunnel (3.2 mm in diameter), and the ligaments were sutured to the periostium around the lateral side of the knee in five rabbits (Fig. 8). An MCL gap injury model of five rabbits was used for control. Then 12 weeks after MCL reconstruction, five rabbits in each group were sacrificed and bone–ligament–bone complex was dissected for testing. During mechanical testing, samples were carefully kept moist by physiological saline solution. Failure load of tissue engineered ligament was recovered to 60 per cent of that in normal MCL (Fig. 9). The mode of failure of the engineered ligament was avulsion from bone tunnel in two samples. The failure mode of the other three samples was midsubstance tear. On the other hand, all the MCL scar failed at midsubstance. These results indicate that engineered ligament substance was stronger than the failure load of the experimental results. On the other hand, the lack of integration to the bony attachment of the grafted engineered ligament needs to be improved. For example, the initial fixation method to the bone tunnel could be changed from suture to button fixation, which is the same as the human ligament reconstruction.

Fig. 8 Macroscopic photograph (haematoxylin and eosin staining) of coronal section of MCL reconstruction using a chitosan–0.1 per cent HA hybrid-polymer fibre scaffold seeded with fibroblasts. After MCL removal, an engineered ligament was placed through the bone tunnel (3.2 mm in diameter). Both ends of the ligament were sutured to the periostium

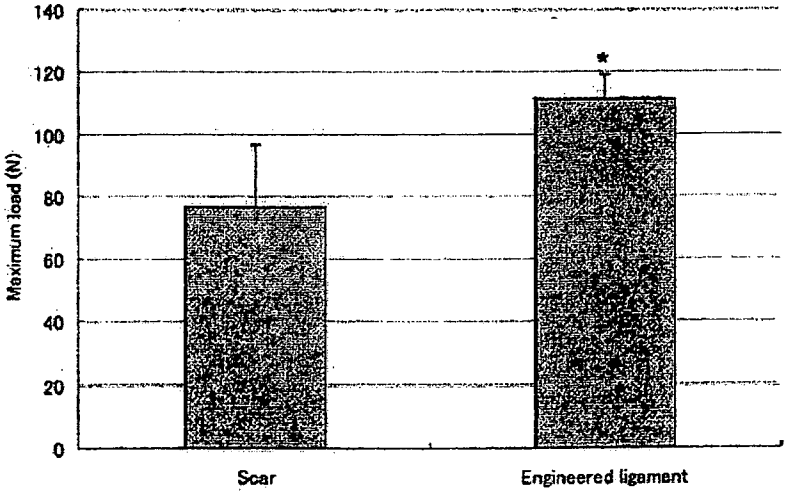

Fig. 9 Maximum failure load of scar and engineered ligament (the data are shown as the mean ± standard deviation ($n = 5$)): *, $p < 0.05$

5 DISCUSSION

Chitosan has been well accepted as a scaffold material in the field of musculoskeletal tissue engineering. Although several basic studies have demonstrated the tissue regeneration potential of GAG-augmented chitosan hydrogels [28, 29], these hydrogels do not have the required mechanical strength for a scaffold material for ligament tissue engineering. To overcome this limitation, a novel polymer fibre was developed as a fundamental scaffold material for ligament and tendon regeneration.

HA enhances the mechanical strength of the polymer fibres. HA also showed superior biological effects on the fibroblasts in a three-dimensional culture system. Chitosan is a cationic polysaccharide consisting of glucosamine residues and HA displays anionic behaviour. Therefore, the increase in mechanical strength in the novel hybrid fibre is this tight-interaction polyion complex effect between chitosan and HA polymers.

In ligament and tendon tissue engineering, it should be considered that the ligament and tendon are subjected to excessive mechanical stress. To maintain the number of attached fibroblasts under these circumstances, a highly cellular adhesive potential is essential for ligament and tendon scaffold materials. Therefore, the focus was on enhancing the cell adhesive potential of the novel material. Zimmerman *et al.* [30] showed that HA is an adhesion modulator molecule, which can mediate the early stage of cell–substrate interaction. Hu *et al.* [13] stated that HA material has positive advantages for fibroblast adhesion. Based on these previous data and the current results, it seems reasonable to conclude that scaffold biomaterials introducing HA provide adequate fibroblast adhesive activity. CD44, a transmembrane glycoprotein expressed in a variety of cell types in connective tissues, is well known as the principal cell-surface receptor for HA. The interaction of CD44 and HA plays a crucial role in regulating cellular activities, including cell–matrix adhesion, cell proliferation, cell migration, and ECM products. As CD44 is a major cell-surface protein in fibroblasts [31], the isolated fibroblasts from ligaments and tendons would increase in CD44 expression. It has been clarified that there was a significant increase in the expression of CD44 and syndecan-4 messenger ribonucleic acids (mRNAs) during cell isolation from the tendon [32]. The switch from monolayer culture to three-dimensional culture also induced a dramatic increase in the expression of CD44 and syndecan-4 mRNAs. The interaction of CD44 on the isolated fibroblast and HA on the scaffold material could provide excellent biological effects on the cultured fibroblast.

There are several limitations in our study. First, the biodegradability and biocompatibility of the scaffold material should be clarified more for the purpose of clinical use. Concerning the biodegradation, 30 per cent of the original strength was maintained 4 weeks after incubation in a culture medium. The hybrid-polymer fibres in this study can be fabricated to obtain the desirable mechanical strength and shape. For example, the failure load of 70 000 fibres will be approximately 10 000 N in the dry condition. The diameter of 70 000 fibres will be 8 mm. This diameter is almost the same as the anterior cruciate ligament in knee joint. After cultivation, the material strength of the scaffold may decrease to 3000 N without ECM apposition. This is about 150 per cent of the failure load in the anterior cruciate ligament; the ultimate load of young anterior cruciate ligament is 2160 N [33]. Concerning the biocompatibility, chitosan has been employed as an excellent biocompatible material for wound healing and tissue repair. On the other hand, immunological reactions of chitosan have been reported. Further observation must be made to confirm the long-term general or local immune reaction. Second, it is well known that the gap between the fabricated scaffold fibres strongly affects fibroblast invasion and angiogenesis into the three-dimensional scaffold. It is necessary to design a better scaffold material with adequate gap between the fabricated fibres for these purposes. Furthermore, studies of surgical methods to enhance the mechanical strength of junction between the scaffold and bone are needed.

For cartilage tissue engineering, the ideal cell-carrier substance is one that closely mimics the natural environment in the cartilage ECM. GAGs, which are parts of the cartilage ECM components, play an important role in regulating expression of the chondrocyte phenotype and in supporting chondrogenesis [34–36]. Therefore, the application of HA as a component of the cartilage scaffold biomaterial must be a reasonable approach for enhancing chondrogenesis. HA has a biological advantage for cartilage tissue engineering. The present scaffold material has the potential to support the chondrogenesis to maintain the chondrocyte phenotype through the process of cartilage regeneration. Furthermore, the present scaffold has a mechanical advantage. In articular cartilage tissue engineering, the fact that articular cartilage is subject to compression and shear stress must be considered. Therefore, to maintain the initial shape of the engineered cartilage and the number of attached chondrocytes, an

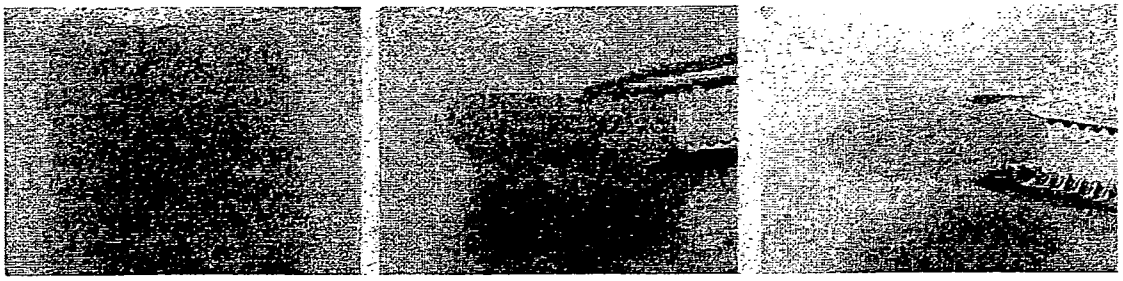

Fig. 10 Cartilage tissue engineered using chitosan-based 0.1 per cent HA hybrid-polymer fibre scaffold (10 mm square and 2 mm in thickness) on which chondrocytes (1×10^6 cells on to the scaffold) were seeded and cultured in a bioreactor for 8 weeks

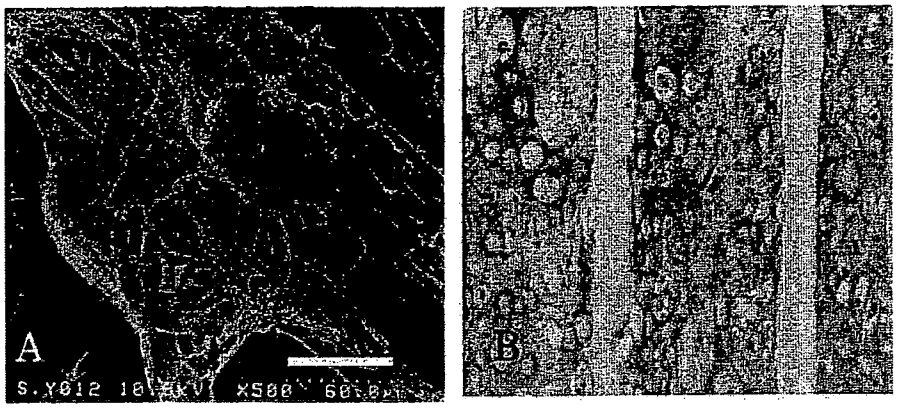

Fig. 11 *In-vitro* engineered cartilage-like tissue: (A) scanning electron micrograph (the bar indicates 60 μm); (B) immunohistochemical staining of type II collagen (magnification, ×400)

adequate mechanical strength and a highly cellular adhesive potential are requirements for scaffold materials. For these reasons, attempts are being made to apply the present scaffold for cartilage tissue engineering [37] in addition to application for tendon and ligament tissue engineering (Fig. 10). Scanning electron microscopy observation of the cultured hybrid-polymer materials showed that chondrocytes proliferated while maintaining their morphological phenotype with a rich extracellular matrix synthesis around the cells (Fig. 11(a)). Immunohistochemical staining with an anti-type II collagen antibody demonstrated rich production of the type II collagen in the pericellular matrix from the chondrocytes (Fig. 11(b)). Further research is needed to determine the adequate shape, pore size, and mechanical properties of a three-dimensional fabrication for cartilage tissue regeneration. A long-term large-animal *in-vivo* study is ongoing.

REFERENCES

1 **Heikel, H. V. A.** Rupture of the rotator cuff of the shoulder: experiences of surgical treatment. *Acta Orthop. Scandinavia*, 1968, **39**, 477–492.
2 **Beynnon, B. D., Johnson, R. J., Abate, J. A., Fleming, B. C.,** and **Nichols, C. E.** Treatment of anterior cruciate ligament injuries, Part 1. *Am. J. Sports Medicine*, 2005, **33**, 1579–1602.
3 **Langer, R.** and **Vacanti, J. P.** Tissue engineering. *Science*, 1993, **260**, 920–926.
4 **Hynes, R. O.** Cell adhesion: old and new questions. *Trends Cell Biology*, 1999, **9**, M33–M37.
5 **Gentleman, E., Lay, A. N., Dickerson, D. A., Nauman, E. A., Livesay, G. A.,** and **Dee, K. C.** Mechanical characterization of collagen fibers and scaffolds for tissue engineering. *Biomaterials*, 2003, **24**, 3805–3813.
6 **Dunn, M. G., Liesch, J. B., Tiku, M. L.,** and **Zawadsky, J. P.** Development of fibroblast-seeded ligament analogs for ACL reconstruction. *J. Biomed. Mater. Res.*, 1995, **29**, 1363–1371.

7 **Huang, D., Chang, T. R., Aggarwal, A., Lee, R. C.,** and **Ehrlich, H. P.** Mechanisms and dynamics of mechanical strengthening in ligament-equivalent fibroblast-populated collagen matrices. *Ann. Biomed. Engng*, 1993, **21**, 289–305.

8 **Ibarra, C., Cao, Y.,** and **Kim, T. H.** Tissue engineering ligaments. *Surg. Forum*, 1996, **47**, 612–615.

9 **Quteish, D., Singh, G.,** and **Dolby, A. E.** Development and testing of a human collagen graft material. *J. Biomed. Mater. Res.*, 1990, **24**, 749–760.

10 **Koski, J. A., Ibarra, C.,** and **Rodeo, S. A.** Tissue-engineered ligament. *Orthop. Clin. North. Am.*, 2000, **31**, 437–452.

11 **Zhu, H., Ji, J., Lin, R., Gao, C., Feng, L.,** and **Shen, J.** Surface engineering of poly (D,L-lactic acid) by entrapment of chitosan-based derivatives for the promotion of chondrogenesis. *J. Biomed. Mater. Res.*, 2002, **62**, 532–539.

12 **Roy, F., DeBlois, C.,** and **Doillon, C. J.** Extracellular matrix analogs as carriers for growth factors: *in vitro* fibroblast behavior. *J. Biomed. Mater. Res.*, 1993, **27**, 389–397.

13 **Hu, M., Sabelman, E. E., Lai, S., Timek, E. K., Zhang, F., Hentz, V. R.,** and **Lineaweaver, W. C.** Polypeptide resurfacing method improves fibroblast's adhesion to hyaluronan strands. *J. Biomed. Mater. Res.*, 1999, **47**, 79–84.

14 **Huang, L., Cheng, Y. Y., Koo, P. L., Lee, K. M., Qin, L., Cheng, J. C.,** and **Kumta, S. M.** The effect of hyaluronan on osteoblast proliferation and differentiation in rat calvarial-derived cell cultures. *J. Biomed. Mater. Res.*, 2003, **66**, 880–884.

15 **Lokeshwar, V. B., Iida, N.,** and **Bourguignon, L. Y. W.** The cell adhesion molecule, GP116, is a new CD44 variant (ex14/v10) involved in hyaluronic acid binding and endothelial cell proliferation. *J. Biol. Chemistry*, 1996, **271**, 23 853–23 864.

16 **Huang, J., He, H., Sheng, L.,** and **Gu, G.** Comparison of calcium alginate film with collagen membrane for guide bone regeneration in mandibular defects in rabbits. *J. Oral Maxillofacial Surg.*, 2002, **60**, 1449–1454.

17 **Dar, A., Shachar, M., Leor, J.,** and **Cohen, S.** Optimization of cardiac cell seeding and distribution in 3D porous alginate scaffolds. *Biotechnol. Bioengng*, 2002, **80**, 305–312.

18 **Degim, Z., Celebi, N., Sayan, H., Babul, A., Erdogan, D.,** and **Take, G.** An investigation on skin wound healing in mice with a taurine–chitosan gel formation. *Amino Acids*, 2002, **22**, 187–198.

19 **Peh, K., Khan, T.,** and **Ching, H.** Mechanical, bioadhesive strength and biological evaluations of chitosan films for wound dressing. *J. Pharm. Sci.*, 2000, **3**, 303–311.

20 **Tamura, H., Tsuruta, Y.,** and **Tokura, S.** Preparation of chitosan-coated alginate filament. *Mater. Sci. Engng*, 2002, **C20**, 143–147.

21 **Majima, T., Funakoshi, T., Iwasaki, N., Yamane, S., Minami, A., Harada, N., Nonaka, S., Maekawa, N., Tamura, Y., Tokura, S., Monde, K.,** and **Nishimaura, S.** Alginate and chitosan polyion complex fibers for scaffold in ligament tissue engineering. *J. Orthop. Sci.*, 2005, **10**, 302–307.

22 **Funakoshi, T., Majima, T., Iwasaki, N., Yamane, S., Masuko, T., Minami, A., Harada, K.,** and **Nishimura, S.** Novel chitosan-based hyaluronan hybrid polymer fibers for a scaffold in ligament tissue engineering. *J. Biomed. Mater. Res.*, 2005, **74**, 338–346.

23 **Nishimura, S., Nishi, N.,** and **Tokura, S.** Adhesion behavior of murine lymphocytes on the surface of fibrous chitin and its derivatives. *Int. J. Biol. Macromolecules*, 1985, **7**, 100–104.

24 **Iwasaki, N., Yamane, S. T., Majima, T., Kasahara, Y., Minami, A., Harada, K., Nonaka, S., Maekawa, N., Tamura, H., Tokura, S., Shiono, M., Monde, K.,** and **Nishimura, S.** Feasibility of polysaccharide hybrid materials for scaffolds in cartilage tissue engineering: evaluation of chondrocyte adhesion to polyion complex fibers prepared from alginate and chitosan. *Biomacromolecules*, 2004, **5**, 828–833.

25 **Funakoshi, T., Majima, T., Iwasaki, N., Yamane, S., Masuko, T., Minami, A., Harada, K.,** and **Nishimura, S.** Application of tissue engineering techniques for rotator cuff regeneration using a chitosan-based hyaluronan hybrid fiber scaffold. *Am. J. Sports Medicine*, 2005, **33**, 1193–1201.

26 **Majima, T., Marchuk, L. L., Sciore, P., Shrive, N. G., Frank, C. B.,** and **Hart, D. A.** Compressive compared with tensile loading of medial collateral ligament scar *in vitro* uniquely influences m-RNA levels for aggrecan, collagen type II and collagenase. *J. Orthop. Res.*, 2000, **18**, 524–531.

27 **Majima, T., Lo, I. K. Y., Marchuk, L. L., Shrive, N. G.,** and **Frank, C. B.** Effects of ligament repair on laxity and creep behaviour of an early healing ligament scar. *J. Orthop. Sci.*, 2006, **11**, 272–277.

28 **Sechriest, V. F., Miao, Y. J., Niyibizi, C., Westerhausen-Larson, A., Matthew, H. W., Evans, C. H., Fu, F. H.,** and **Suh, J. K.** GAG-augmented polysaccharide hydrogel: a novel biocompatible and biodegradable material to support chondrogenesis. *J. Biomed. Mater. Res.*, 2000, **49**, 534–541.

29 **Suh, J. K.** and **Matthew, H. W.** Application of chitosan-based polysaccharide biomaterials in cartilage tissue engineering: a review. *Biomaterials*, 2000, **21**, 2589–2598.

30 **Zimmerman, E., Geiger, B.,** and **Addadi, L.** Initial stages of cell–matrix adhesion can be mediated and modulated by cell-surface hyaluronan. *Biophys. J.*, 2002, **82**, 1848–1857.

31 **Holifield, B. F.** and **Jacobson, K.** Mapping trajectories of Pgp-1 membrane protein patches on surfaces of motile fibroblasts reveals a distinct boundary separating capping on the lamella and forward transport on the retracting tail. *J. Cell Sci.*, 1991, **98**, 191–203.

32 **Sawaguchi, N., Majima, T., Iwasaki, N., Funakoshi, T., Shimode, K., Onodera, T.,** and **Minami, A.** Extracellular matrix modulates expression of cell-surface proteoglycan genes in fibroblasts. *Connective Tissue Res.*, 2006, **47**, 141–148.

33 **Woo, S. L.-Y., Hollis, J. M., Adams, D. J., Lyon, R. M.,** and **Takai, S.** Tensile properties of the human femur–anterior cruciate ligament–tibia complex. The effects of specimen age and orientation. *Am. J. Sports Medicine*, 1991, **19**, 217–225.

34 **Kato, Y., Mukudai, Y., Okimura, A., Shimazu, A.,** and **Nakamura, S.** Effect of hyaluronic acid on the release of cartilage matrix proteoglycan and fibronectin from the cell matrix layer of chondrocyte cultures: interactions between hyaluronic acid and chondroitin sulfate glycosaminoglycan. *J. Rheumatology*, 1995, **43**(Suppl.), 158–159.

35 **Shimazu, A., Jikko, A., Iwamoto, M., Koike, T., Yan, W., Okada, Y., Shinmei, M., Nakamura, S.,** and **Kato, Y.** Effect of hyaluronic acid on the release of the proteoglycan from the cell matrix in rabbit chondrocyte culture in the presence and absence of cytokines. *Arthritis Rheum.*, 1993, **36**, 247–253.

36 **Larsen, N. E., Lombad, K. M., Parent, E. G.,** and **Balazs, E. A.** Effect of hyaluroan on cartilage and chondrocyte cultures. *J. Orthop. Res.*, 1992, **10**, 23–32.

37 **Yamane, S., Iwasaki, N., Majima, T., Funakoshi, T., Masuko, T., Harada, K., Minami, A., Monde, K.,** and **Nishimura, S.** Feasibility of chitosan-based hyaluronic acid hybrid biomaterial for a novel scaffold in cartilage tissue engineering. *Biomaterials*, 2005, **26**, 611–619.

Acta Crystallographica Section F
Structural Biology and Crystallization Communications
ISSN 1744-3091

Crystallization and preliminary crystallographic analysis of the Tob–hCaf1 complex

Kinya Nishida,[a,b] Masataka Horiuchi,[a] Nobuo N. Noda,[a] Kiyohiro Takahasi,[a] Norimasa Iwasaki,[b] Akio Minami[b] and Fuyuhiko Inagaki[a]*

[a]Department of Structural Biology, Graduate School of Pharmaceutical Science, Hokkaido University, N12, W6, Kita-ku, Sapporo 060-0812, Japan, and [b]Department of Orthopaedic Surgery, Graduate School of Medicine, Hokkaido University, N15, W7, Kita-ku, Sapporo 060-8638, Japan

Correspondence e-mail: finagaki@pharm.hokudai.ac.jp

Received 9 September 2007
Accepted 9 November 2007

The Tob/BTG family is a group of antiproliferative proteins that contain two highly homologous regions named Box A and Box B. These proteins all associate with CCR4-associated factor 1 (Caf1), which belongs to the ribonuclease D family of deadenylases. The antiproliferative region of human Tob (residues 1–138) and intact hCaf1 were co-expressed in *Escherichia coli*, purified and successfully cocrystallized. The crystal belongs to the tetragonal space group *I*422, with unit-cell parameters $a = b = 150.9$, $c = 113.9$ Å, and is estimated to contain one heterodimer per asymmetric unit. The crystal diffracted to around 2.6 Å resolution.

1. Introduction

The Tob/BTG family is a group of antiproliferative proteins (Tirone, 2001; Matsuda *et al.*, 2001). This family consists of Tob (Matsuda *et al.*, 1996), Tob2 (Ikematsu *et al.*, 1999), BTG1 (Rouault *et al.*, 1992), BTG2/Tis21/PC3 (Rouault *et al.*, 1996; Fletcher *et al.*, 1991; Bradbury *et al.*, 1991), PC3B (Buanne *et al.*, 2000) and ANA/BTG3 (Yoshida *et al.*, 1998; Guehenneux *et al.*, 1997) in mammalian cells. These proteins have been reported to inhibit cell proliferation when expressed exogenously in cultured cells. The N-terminal region of the Tob/BTG-family proteins is thought to be responsible for the antiproliferative function since it is highly conserved. This region includes two homologous regions named Box A and Box B (Guehenneux *et al.*, 1997). The Tob/BTG-family proteins are involved in cell-cycle regulation in a variety of cells, such as T lymphocytes, osteoblasts, fibroblasts, epithelial cells, neuronal cells and germ cells. For example, in mice defective in *tob* the rate of occurrence of tumours in the lungs, liver and lymph nodes is higher than that in wild-type mice (Yoshida *et al.*, 2003) and levels of *tob* expression are often decreased in human lung cancers (Yoshida *et al.*, 2003).

The antiproliferative activities of the Tob/BTG-family proteins are a consequence of their association with target proteins in cells. Much evidence has been accumulated that suggests that CCR4-associated factor 1 (Caf1), also known as Cnot7, is a common binding partner for Tob/BTG family proteins (Prévôt *et al.*, 2001; Ikematsu *et al.*, 1999; Bogdan *et al.*, 1998; Rouault *et al.*, 1998). Caf1 is a component of the CCR4–NOT deadenylase complex and is involved in deadenylation of the poly(A) tail of mRNA, which is the first major step in mRNA degradation in eukaryotes (Parker & Song, 2004; Meyer *et al.*, 2004). Tob interacts with Caf1 and poly(A)-binding protein (PABP) simultaneously, thus enhancing mRNA degradation through recruiting the CCR4–NOT complex to stimulate deadenylation (Ezzeddine *et al.*, 2007).

The recognition between Tob and Caf1 is critical for deadenylation and antiproliferative activities. In this report, we describe the expression, purification, crystallization and preliminary crystallographic analysis of the Tob–hCaf1 complex.

Table 1
Data-collection statistics.

Values in parentheses are for the last shell.

	Native	$NdCl_3$ soak	Methylmercuric acetate soak	SeMet derivative
Wavelength (Å)	1.0000	1.0000	1.0000	1.0000
Temperature (K)	100	100	100	100
Space group	*I*422	*I*422	*I*422	*I*422
Unit-cell parameters (Å, °)	$a = b = 150.9$, $c = 113.9$, $\alpha = \beta = \gamma = 90$	$a = b = 151.9$, $c = 114.1$, $\alpha = \beta = \gamma = 90$	$a = b = 152.2$, $c = 114.7$, $\alpha = \beta = \gamma = 90$	$a = b = 151.5$, $c = 114.0$, $\alpha = \beta = \gamma = 90$
Resolution (Å)	58–2.6 (2.7–2.6)	76–3.1 (3.3–3.1)	48–4.0 (4.2–4.0)	59–2.7 (2.9–2.7)
Measured reflections	141379	87455	39768	263973
Unique reflections	19646	11705	5937	18504
Completeness (%)	97.9 (98.9)	94.9 (94.9)	99.9 (99.9)	99.9 (99.9)
$I/\sigma(I)$	5.6 (2.4)	4.3 (2.3)	6.7 (5.0)	3.5 (2.1)
R_{merge}†	0.103 (0.268)	0.132 (0.270)	0.095 (0.128)	0.133 (0.227)

† $R_{merge} = \sum_{hkl} \sum_i |I_i(hkl) - \overline{I(hkl)}| / \sum_{hkl} \sum_i I_i(hkl)$, where $I_i(hkl)$ is the observed intensity and $\overline{I(hkl)}$ is the average intensity over symmetry-equivalent measurements.

2. Expression and purification

In order to elucidate the antiproliferative activity of Tob, the antiproliferative region of human Tob comprising the amino-terminal 138 residues (which we refer to as TobN138) and intact hCaf1 were co-expressed in *Escherichia coli*. The gene of TobN138 was subcloned under a hexahistidine tag (6His) into the pET-28 plasmid and the gene for hCaf1 was subcloned into the pET-11 plasmid (Novagen). These plasmids were co-transformed in *E. coli* BLR (DE3) pLysS for native proteins and the methionine-auxotroph strain B834 (DE3) for SeMet-labelled proteins. Cells were cultured to an OD_{600} of 0.5 at 303 K and induced with 1 m*M* isopropyl β-D-1-thiogalactopyranoside for 18 h. After cell lysis, the protein was applied onto Ni–NTA agarose resin (Qiagen) and eluted with a gradient of 0–250 m*M* imidazole in 50 m*M* Tris–HCl pH 8.0, 150 m*M* NaCl and 1 m*M* ABSF. The 6HisTobN138–Caf1 complex was separated from 6HisTobN138 monomer using a Superdex 75pg 26/60 gel-filtration column (Amersham) equilibrated with 50 m*M* Tris–HCl pH 8.0, 150 m*M* NaCl and 0.5 m*M* EDTA. The heterodimer fraction was loaded onto a Mono Q HR10/10 anion-exchange column (Amersham) equilibrated with 20 m*M* Tris–HCl pH 8.0. The heterodimer was eluted using a 160 ml linear gradient of 0–1 *M* NaCl. Fractions containing the heterodimer were dialyzed against 10 m*M* Tris–HCl pH 8.0, 30 m*M* NaCl, 0.1 m*M* EDTA and 5 m*M* dithiothreitol (DTT) and stored at 193 K prior to crystallization. To determine the amino-terminal sequences and molecular weights of 6HisTobN138 and hCaf1, the proteins were separated using a Poros R2/M reverse-phase column (Applied Biosystems). The protein sequences determined using a PPSQ-21 protein sequencer (Shimazu) indicated that the N-terminal methionine was removed from both the 6HisTobN138 and hCaf1 proteins. The molecular weights of 6HisTobN138 and hCaf1 were determined to be 18 736 Da (calculated molecular weight 18 733 Da) and 32 617 Da (calculated molecular weight 32 613 Da), respectively, using a Voyager DE-PRO MALDI–TOF mass spectrometer (Applied Biosystems). The purified protein complex was concentrated to 20 mg ml^{-1} and used for crystallization (Fig. 1).

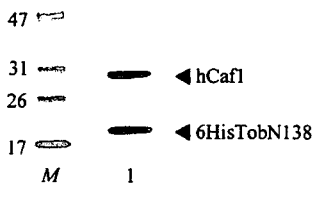

Figure 1
SDS–PAGE of 6HisTobN138–hCaf1 complex (lane 1) on 5–20% gradient gel. Lane *M* contains molecular-weight markers (labelled in kDa). Proteins were stained with Coomassie Brilliant Blue.

3. Crystallization

Initial crystallization conditions for native and SeMet-labelled protein complexes were obtained by sparse-matrix screening (Hampton, Aliso Viejo, California, USA). In the sitting-drop vapour-diffusion method, 1 µl 20 mg ml^{-1} 6HisTobN138–hCaf1 complex (10 m*M* Tris–HCl pH 8.0, 30 m*M* NaCl, 0.1 m*M* EDTA and 5 m*M* DTT) was mixed with an equal volume of reservoir solution [80 m*M* Tris–HCl pH 8.0, 160 m*M* sodium acetate, 10 m*M* DTT, 12%(*w*/*v*) PEG 4000 and 12% glycerol]. The protein/reservoir mixture was equilibrated against 100 µl reservoir solution at 293 K and small crystals (<0.02 mm) were obtained after 24 h. To prepare the seed stock, 1 µl of a drop containing small crystals was diluted with 30 µl of the same reservoir solution and vortexed with a Teflon ball (Hampton) in a microtube. 1 µl of serial dilutions (10^{-1}-fold to 10^{-8}-fold) of seed stock was mixed with 1 µl 20 mg ml^{-1} protein solution and equilibrated against 100 µl reservoir solution at 293 K. After 48 h at 293 K, microseeding generated crystals of dimensions 0.3 × 0.3 × 0.1 mm (Fig. 2). To prepare heavy-atom derivatives, crystals were soaked at 293 K in reservoir solutions without DTT and EDTA that contained either 1 m*M* neodymium chloride (for 20 h) or 0.1 m*M* methylmercuric acetate (for 1 h).

4. Preliminary X-ray analysis

All diffraction data for the 6HisTobN138–Caf1 complex were collected at 100 K using synchrotron radiation with a PX210 CCD detector (Oxford) at the Osaka University beamline BL44XU in SPring-8. Prior to data collection, the crystal was cryoprotected by

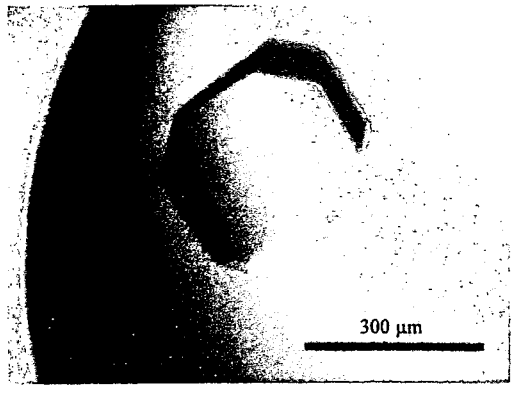

Figure 2
Crystal of 6HisTobN138–hCaf1 complex. The scale bar is 300 µm in length.

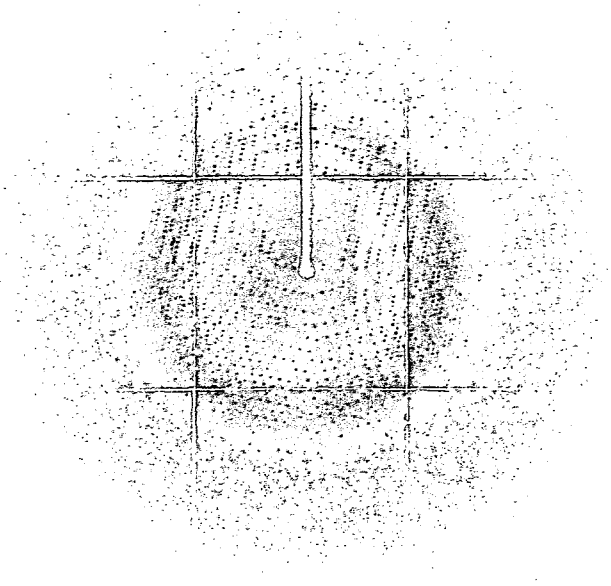

Figure 3
Diffraction pattern of 6HisTobN138–hCaf1.

incubation for 5 min in reservoir solution containing 15% PEG 4000 and 30% glycerol. After soaking, the crystals were mounted in cryoloops (Hampton) and frozen in liquid nitrogen. Diffraction data were processed using the program *MOSFLM* (Leslie, 1992) and intensities were scaled using *SCALA* from the *CCP*4 program suite (Collaborative Computational Project, Number 4, 1994) and *HKL*-2000 (Otwinowski & Minor, 1997; Fig. 3). The diffraction data statistics are shown in Table 1. The crystal belonged to the tetragonal space group *I*422, with unit-cell parameters $a = b = 150.9$, $c = 113.9$ Å. The acceptable range of the volume-to-weight ratio (V_M) value (Matthews, 1968) indicates that the crystal contains one heterodimer per asymmetric unit (the V_M value is 3.16 Å^3 Da^{-1}). The solvent content of the crystal was estimated as 61%. The phases were determined by the multiple isomorphous replacement method using crystals of heavy-atom derivatives and SeMet-labelled protein. The crystal structure was recently determined and will be described elsewhere (PDB code 2d5r).

We thank Dr Atsushi Nakagawa, Dr Eiki Yamashita and all the staff of the BL44XU Macromolecule Assemblies of Osaka University for assistance with X-ray data collection. This work was supported by CREST of Japan Science and Technology (JST), Grants-in-Aid for scientific research (15770063 and 16017203) and the National Project on Protein Structural and Functional Analyses from the Ministry of Education, Culture, Sports, Science and Technology (MEXT), Japan.

References

Bogdan, J. A., Burton, C. A., Pedicord, D. L., Sukovich, D. A., Benfield, P. A., Corjay, M. H., Stoltenborg, J. K. & Dicker, I. B. (1998). *Biochem. J.* **336**, 471–481.
Bradbury, A., Possenti, R., Shooter, E. M. & Tirone, F. (1991). *Proc. Natl Acad. Sci. USA*, **88**, 3353–3357.
Buanne, P., Corrente, G., Micheli, L., Palena, A., Lavia, P., Spadafora, C., Lakshmana, M. K., Rinaldi, A., Banfi, S., Quarto, M., Bulfone, A. & Tirone, F. (2000). *Genomics*, **68**, 253–263.
Collaborative Computational Project, Number 4 (1994). *Acta Cryst.* D**50**, 760–763.
Ezzeddine, N., Chang, T. C., Zhu, W., Yamashita, A., Chen, C. Y., Zhong, Z., Yamashita, Y., Zheng, D. & Shyu, A. B. (2007). *Mol. Cell. Biol.* **27**, 7791–8001.
Fletcher, B. S., Lim, R. W., Varnum, B. C., Kujubu, D. A., Koski, R. A. & Herschman, H. R. (1991). *J. Biol. Chem.* **266**, 14511–14518.
Guehenneux, F., Duret, L., Callanan, M. B., Bouhas, R., Hayette, S., Berthet, C., Samarut, C., Rimokh, R., Birot, A. M., Wang, Q., Magaud, J. P. & Rouault, J. P. (1997). *Leukemia*, **11**, 370–375.
Ikematsu, N., Yoshida, Y., Tsuzuku, J. K., Ohsugi, M., Onda, M., Hirai, M., Fujimoto, J. & Yamamoto, T. (1999). *Oncogene*, **18**, 7432–7441.
Leslie, A. G. W. (1992). *Jnt CCP4/ESF–EACBM Newsl. Protein Crystallogr.* **26**.
Matsuda, S., Rouault, J. P., Magaud, J. P. & Berthet, C. (2001). *FEBS Lett.* **497**, 67–72.
Matsuda, S., Tsuzuku, J. K., Ohsugi, M., Yoshida, M., Emi, M., Nakamura, Y., Onda, M., Yoshida, Y., Nishiyama, A. & Yamamoto, T. (1996). *Oncogene*, **12**, 705–713.
Matthews, B. W. (1968). *J. Mol. Biol.* **33**, 491–497.
Meyer, S., Temme, C. & Wahle, E. (2004). *Crit. Rev. Biochem. Mol. Biol.* **39**, 197–216.
Otwinowski, Z. & Minor, W. (1997). *Methods Enzymol.* **276**, 307–326.
Parker, R. & Song, H. (2004). *Nature Struct. Mol. Biol.* **11**, 121–127.
Prévôt, D., Morel, A. P., Voeltzel, T., Rostan, M. C., Rimokh, R., Magaud, J. P. & Corbo, L. (2001). *J. Biol. Chem.* **276**, 9640–9648.
Rouault, J. P. *et al.* (1996). *Nature Genet.* **14**, 482–486.
Rouault, J. P., Prévôt, D., Berthet, C., Birot, A. M., Billaud, M., Magaud, J. P. & Corbo, L. (1998). *J. Biol. Chem.* **273**, 22563–22569.
Rouault, J. P., Rimokh, R., Tessa, C., Paranhos, G., Ffrench, M., Duret, L., Garoccio, M., Germain, D., Samarut, J. & Magaud, J. P. (1992). *EMBO J.* **11**, 1663–1670.
Tirone, F. (2001). *J. Cell. Physiol.* **187**, 155–165.
Yoshida, Y. *et al.* (2003). *Genes Dev.* **17**, 1201–1206.
Yoshida, Y., Matsuda, S., Ikematsu, N., Tsuzuku, J. K., Inazawa, J., Umemori, H. & Yamamoto, T. (1998). *Oncogene*, **16**, 2687–2693.

Clin Rheumatol (2007) 26: 515–519
DOI 10.1007/s10067-006-0318-y

ORIGINAL ARTICLE

Takashi Kitamura · Jun Hashimoto · Tsuyoshi Murase · Tetsuya Tomita · Takako Hattori · Hideki Yoshikawa · Kazuomi Sugamoto

Radiographic study of joint destruction patterns in the rheumatoid elbow

Received: 7 January 2006 / Revised: 1 April 2006 / Accepted: 3 April 2006 / Published online: 3 May 2006

Abstract Knowledge of the pattern of joint destruction is important for planning the therapeutic approach to rheumatoid arthritis (RA) of the elbow. Accordingly, we carried out a large-scale radiographic study with the objective of elucidating the joint destruction pattern in rheumatoid elbows. From 2001 through 2003, we examined and took plain X-rays of both elbows of 193 RA patients (i.e., 386 elbows), consisting of 18 men and 175 women, with a mean age of 57.0 years. Radiographic images of the elbow joints were used to classify the degree of bone loss in various zones on the elbow joint surface into four grades of severity, and joint destruction was compared between the left and right elbows. In addition, correlation in the extent of bone loss between each of the zones of the same elbow and differences in the extent of bone loss were analyzed statistically. The results showed direct correlations for destruction of the elbow joint surface among the zones for the left and right elbow joints and in the same elbow joint. However, more severe destruction was observed on the radial side of the humeral trochlea, and it was surmised that destruction of the elbow joint must begin at that site and gradually spread mediolaterally. In addition, in the same elbow joint, the correlation in the degree of bone loss between the trochlea of humerus and the trochlear notch was especially strong, indicating that the bone destruction at both sites represented mirror lesions. We conclude that when performing radiographic diagnosis of the joint damage in the rheumatoid elbow, knowledge of this pattern of joint destruction will be useful for assessing whether there is joint destruction in the initial stage and for deciding the therapeutic approach.

Keywords Elbow joint · Radiography · Rheumatoid arthritis

T. Kitamura (✉)
Department of Orthopedic Surgery, Kaizuka City Hospital,
3-10-20, Hori, Kaizuka,
Osaka 597-0015, Japan
e-mail: kitamura@tb3.so-net.ne.jp
Tel.: +81-0724-225865
Fax: +81-0724-396061

J. Hashimoto · T. Murase · T. Tomita · H. Yoshikawa · K. Sugamoto
Department of Orthopaedics,
Osaka University Medical School,
2-2, Yamadaoka, Suita,
Osaka 565-0871, Japan

T. Hattori
Department of Orthopedic Surgery, NTT West Osaka Hospital,
2-6-40,Karasugatsuji,Tennouji,
Osaka 543-8922, Japan

Introduction

The elbow joint is a common site for the development of rheumatoid arthritis (RA), and it is one of the most important joints in the upper limb as it controls the reach of the hand [1–4]. For this reason, disorders of the elbow joint can seriously interfere with activities of daily living (ADL) of RA patients. In general, when arthropathy is mild, therapy consists of conservative treatments such as drug administration and/or intraarticular injection of steroid. In severe disease, surgical treatments such as synovectomy and artificial elbow joint replacement may be performed [1–4]. For treatment selection and planning, it is very important for the physician to have a good understanding of the pattern of destruction that has occurred in the RA elbow joint. However, it is unfortunate that to date very few reports of analysis of the pattern of bone destruction in RA elbow joints have been published.

We therefore carried out a large-scale radiographic study with the objective of elucidating the pattern of RA elbow joint bone destruction.

Subjects

From 2001 to 2003, we examined plain X-rays of both elbow joints of 233 patients who satisfied the ARA diagnostic criteria. Forty of these patients were excluded from the present study due to previous synovectomy or

artificial elbow joint replacement (33 patients) or because the X-rays were unreadable (seven patients). The remaining 193 RA patients, i.e., 386 elbows, were the subjects of this study. They consisted of 18 men and 175 women, with an age range of 23~84 years (mean 57.0 years). History of drug administration, including steroids, and duration of RA were unclear.

Methods

Radiographic classification of the severity of RA was performed on the basis of plain X-ray anteroposterior images and lateral images of the bilateral elbow joints that were obtained for each patient at the time of final examination. X-rays were taken with the patient in a sitting position. Frontal views were obtained with the elbow joint extended and the forearm in the supine position, while lateral views were obtained with the elbow joint flexed at 90° and the forearm in the intermediate position. The frontal images were divided into three zones: the capitulum of the humerus (zone A), the radial side of the humeral trochlea (zone B), and the ulnar side of the humeral trochlea (zone C). The extent of destruction of the joint surface was determined for each of these zones. In addition, from the lateral view, the extent of joint surface destruction was determined for the olecranon (zone D).

Extent of joint destruction was assessed by reference to a template of the normal elbow joint that had been prepared in advance. The ratings used were grade 0, no bone loss; grade 1, less than 3 mm of bone loss from the joint surface; grade 2, bone loss of 3 to less than 6 mm; and grade 3, bone loss of 6 or more mm (Figs. 1 and 2).

We investigated the extent of bone destruction observed in each of the joint zones, and also investigated whether there was any correlation in destruction among the zones. In practice, we first investigated the correlation in the extent of bone loss in the same zone in both elbows of the same patient, and then compared joint destruction in the left and right elbows. In addition, the correlation in the extent of bone loss among each zone of the same elbow and differences in the extent of bone loss were analyzed statistically.

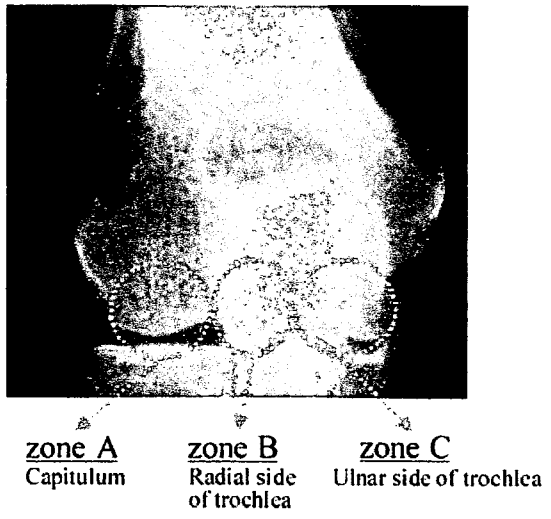

Fig. 1 Radiographic classification (*zones A, B,* and *C*)

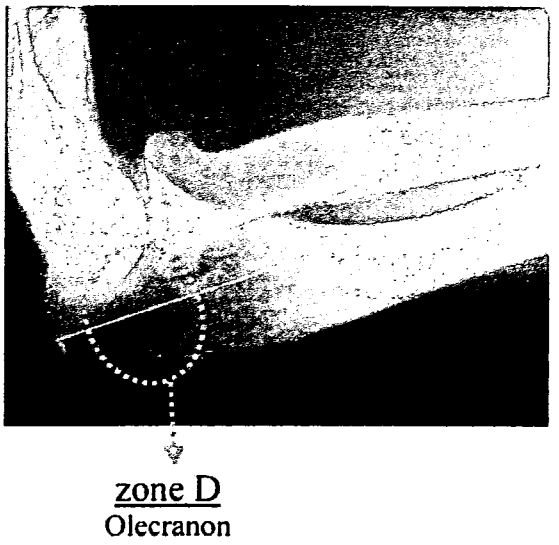

Fig. 2 Radiographic classification (*zone D*)

Spearman's ranked correlation coefficients were used for statistical analyses of correlations, while one-way analysis of variance (ANOVA) and Fisher's least significant difference (LSD) test were used to analyze differences in extent of bone loss.

Results

The extent of bone loss in each zone of the joint as seen on frontal X-ray images was as follows: zone A, 26.2% grade 0, 62.1% grade 1, 8.8% grade 2, and 2.8% grade 3; zone B, 26.2% grade 0, 37.0% grade 1, 26.9% grade 2, and 9.8% grade 3; and zone C, 26.9% grade 0, 62.1% grade 1, 2.6% grade 2, and 8.3% grade 3. The extent of bone loss was therefore similar in zone A and zone C, whereas zone B exhibited a lower percentage rated as grade 2 and a higher percentage rated as grade 3 compared with the other two zones. The extent of bone loss seen on lateral X-ray images (zone D) was grade 0 in 27.2%, grade 1 in 61.1%, grade 2 in 8.3%, and grade 3 in 3.4% (Table 1).

A significant correlation was found for the extent of bone loss in the same zone between the left and right elbows, and correlation was found for bilateral elbow joint destruction (zone A r=0.833, p<0.001; zone B r=0.804, p<0.001; zone C r=0.881, p<0.001; and zone D r=0.887, p<0.001).

In addition, statistically significant correlations were also found for the extent of bone loss among zones in the same elbow (r=0.789~0.951, p<0.001) (Fig. 3). A particularly strong correlation was demonstrated between zone C and zone D (r=0.951, p<0.001).

On the other hand, the extent of bone loss was significantly greater in zone B compared with zone A and zone C (p<0.05), indicating that joint surface

Table 1 Radiographic classification of severity of joint destruction in the elbow (n=193)

Grade	Zone A		Zone B		Zone C		Zone D	
	R/L	Total(%)	R/L	Total(%)	R/L	Total(%)	R/L	Total(%)
0	50/51	26.2	49/52	26.2	51/53	26.9	51/54	27.2
1	123/117	62.2	73/70	37.1	120/120	62.2	117/119	61.1
2	14/20	8.8	54/50	26.9	7/3	2.6	16/16	8.3
3	6/5	2.8	17/21	9.8	15/17	8.3	9/4	3.4
Total	193/193	100	193/193	100	193/193	100	193/193	100

destruction was more advanced in the central part of distal humerus articular surface than at other sites (Fig. 4).

In addition, bone destruction of the humeral trochlea that extended to the olecranon fossa, i.e., a so-called Y-shaped

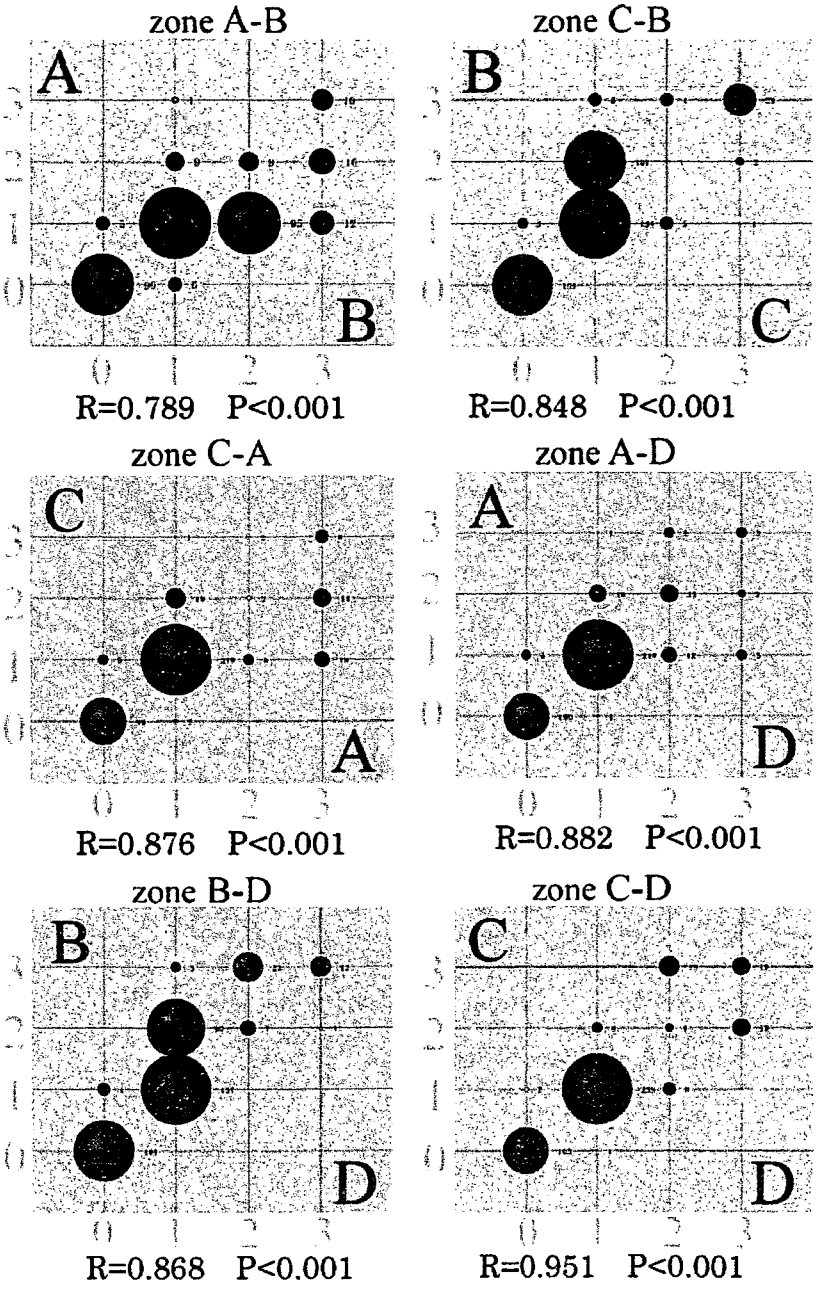

Fig. 3 Correlation of joint destruction among *zonesA, B, C,* and *D* (386 joints)

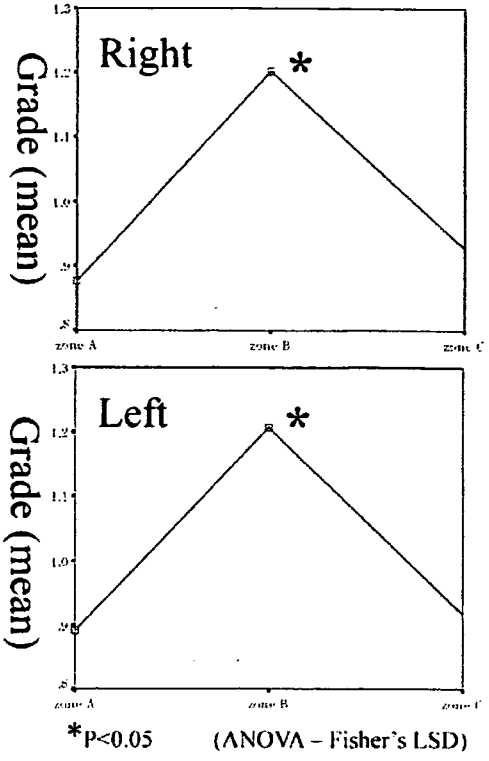

Fig. 4 Distribution of joint destruction grade (*zones A, B,* and *C*)

deformity, was observed in six of the patients, although this was bilateral in only two patients.

Discussion

Larsen's classification, based on the radiological findings for each joint, is widely used as an index of progression of RA disease stage. However, this classification has only two assessment criteria, i.e., the presence/absence of joint space narrowing and the presence/absence of joint surface erosion; the extent of bone loss is not assessed. Accordingly, this classification is said to have poor sensitivity for assessing the extent of joint destruction [5–7]. Lehtinen et al. [7] reported that joint space narrowing in the RA elbow differs from that in weight-bearing joints in that it occurs only subsequent to erosive destruction. They also stated that caution is necessary when using Larsen's classification to assess bone destruction in the elbow because it is a nonweight-bearing joint. In addition, joint destruction in RA is reported to generally show left–right symmetry [5–7]. However, that conclusion has been based only on simple bilateral comparison of the presence/absence of joint destruction, and, to date, there have been no reports of statistical analysis of site and extent of joint destruction. Accordingly, we carried out the present large-scale radiographic study with the objective of elucidating the pattern of bone destruction in the RA elbow joint. To achieve this, we used our own classification system to assess the extent of bone loss in various zones on the elbow joint surface, and joint destruction was compared between the left and right elbows. We then performed statistical analyses to determine whether there were any correlations in the extent of bone loss among each of the zones in the bilateral elbows and in the same elbow.

Our patients showed positive correlations among each of the zones for the extent of bone loss in the same elbow joint, and positive correlations were also found for the extent of joint surface bone loss in the same zones in the bilateral elbows. On the other hand, when we investigated the extent of bone loss in each zone in the same joint, we found it to be significantly greater on the radial side of the humeral trochlea compared with the ulnar side of the trochlea and the capitulum. We therefore surmised that the joint destruction must begin at the radial side of the humeral trochlea and gradually spread mediolaterally. In addition, in the same elbow joint, the correlation in the degree of bone loss between the ulnar side of the trochlea and the olecranon was particularly strong, indicating that the bone destruction at both sites represented symmetrical lesions.

Two theories have been proposed in an attempt to explain the underlying mechanism of the destruction observed in upper limb joints with RA. In the first, the principal cause is considered to be destruction and absorption of cartilage and bone as a result of the actions of cytokines released from the synovial tissue [8, 9]. The second theory holds that the major effects arise from anatomical and/or mechanical factors [10]. Ochi et al. [11] reported that even in the same joint the mechanism of destruction varies widely depending on the disease type. That is, they found that in the type involving damage to the smaller joints, the main bone destruction consisted of erosion of the joint surface due to proliferation of synovitis. Whereas with the mutilating type of arthritis, the main cause of bone destruction was crushing of bone that had become highly osteoporotic because of severe joint instability due to joint laxity.

It is possible that the level of stress applied to the elbow joints differs between the dominant and nondominant arm. However, in the present study, we found no clear left–right difference in the extent of joint destruction, suggesting that the effects of mechanical factors on bone destruction in the RA elbow are slight. Even so, consideration must be given to the fact that most of the patients in our present series were at an earlier stage of the disease, showing a milder degree of joint destruction. Conversely, however, some patients with severe joint destruction, such as is likely to cause the so-called Y-shaped deformity, exhibited clear left–right differences in the extent of damage. Therefore, we cannot rule out the possibility that mechanical factors play a larger role than immunological factors in the advanced stages of joint destruction.

Application of axial compression in the direction of the long axis of the forearm reportedly results in almost equal transmission of the force to the radial joint and the ulnar joint, or slightly greater transmission to the radial joint [12–14]. The surface of the radial side of the humeral trochlea becomes the varus–valgus pivot point of the elbow [15], and for this reason it is possible that when joint laxity occurs due to synovitis, forces are concen-

trated in that area and this leads to the progression of joint destruction.

Our present results indicated the possibility that joint destruction in the RA elbow begins on the radial side of the humeral trochlea and gradually spreads mediolaterally. If we accept the validity of this pattern of destruction of the elbow joint, then when analyzing X-rays taken in the early stage of RA elbow joint damage, it should be possible to focus on the radial side of the humeral trochlea and determine whether joint destruction had already begun. In addition, if bone destruction on the radial side of the trochlea were mild, we would be able to conclude that the joint destruction was at an early stage and that a minimally invasive therapy such as synovectomy was indicated.

The progression of joint destruction can be considered influenced by various factors, such as medication (including NSAIDs, DMARDs, and steroids), disease duration, and progression of joint deformation due to aging or osteoporosis [16–19]. A limitation of the present study was that we were unable to discuss the possible effects of drug treatments, disease duration, and aging in our patient series. However, this is the first report of a statistical analysis of the pattern of joint destruction in the rheumatoid elbow, and we think that our findings will make a significant contribution to decision making regarding therapeutic approaches to RA of the elbow.

References

1. Boyd AD, Thornhill TS (1989) Surgical treatment of the elbow in rheumatoid arthritis. Hand Clin 5(4):645–655
2. Rosenberg GM, Tuner RH (1984) Nonconstrained total elbow arthroplasty. Clin Orthop 187:154–162
3. Linclau LA, Winia WPCA, Korst JK (1983) Synovectomy of the elbow in rheumatoid arthritis. Acta Orthop Scand 54 (6):935–937
4. Pritchard RW (1991) Total elbow joint arthroplasty in patients with rheumatoid arthritis. Semin Arthritis Rheum 21(1):24–29
5. Ljung P, Jonsson K, Rydgren L, Rydholm U (1995) The natural course of rheumatoid elbow arthritis: a radiographic and clinical five-year follow up. J Orthop Rheumatol 8:32–36
6. Lehtinen JT, Kaarela K, Kauppi MJ, Belt EA, Maenpaa HM, Lehto MUK (2002) Bone destruction patterns of the rheumatoid elbow: a radiographic assessment of 148 elbows at 15 years. J Shoulder Elbow Surg 11:253–258
7. Lehtinen JT, Kaarela K, Belt EA, Kauppi MJ, Skytta E, Kuusela PP, Kautiainen HJ, Lehto MUK (2001) Radiographic joint space in rheumatoid elbow joints. A 15-year prospective follow-up study in 74 patients. Rheumatology 40:1141–1145
8. Kirwan JR (1997) The relationship between synovitis and erosions in rheumatoid arthritis. Br J Rheumatol 36:225–228
9. Cuomo F, Greller MJ, Zuckerman JD (1998) The rheumatoid shoulder. Rheum Dis Clin North Am 24:67–82
10. Tan AL, Tanner SF, Conaghan PG, Radjenovic A, O'Connor P, Brown AK, Emery P, McGonagle D (2003) Role of metacarpophalangeal joint anatomic factors in the distribution of synovitis and bone erosion in early rheumatoid arthritis. Arthritis Rheum 48:1214–1222
11. Ochi T, Iwase R, Yonemasu K, Matsukawa M, Yoneda M, Yukioka M, Ono K (1988) Natural course of joint destruction and fluctuation of serum C1q levels in patients with arthritis. Arthritis Rheum 31:37–43
12. Amis AA, Dowson D, Wright V, Miller JH (1979) The derivation of the elbow joint forces and their relation to prosthesis design. J Med Eng Technol 3:229–234
13. Amis AA, Dowson D, Wright V (1980) Elbow joint force predictions for some strenuous isometric actions. J Biomech 13:765–775
14. Halls AA, Travill R (1964) Transmission of pressure across the elbow joint. Anat Rec 150:243–247
15. Morrey BF, An KN, Stormont TJ (1988) Force transmission through the radial head. J Bone Jt Surg 70-A:250–256
16. McIlwain HH (2003) Glucocorticoid-induced osteoporosis: pathogenesis, diagnosis, and management. Prev Med 36:243–249
17. Solomon DH, Levin Elaine, Helfgott SM (2000) Patterns of medication use before and after bone densitometry: factors associated with appropriate treatment. J Rheumatol 27:1496–1500
18. Minaur NJ, Kounail D, Vedi S, Compston JE, Beresford JN, Bhalla K (2002) Methotrexate in the treatment of rheumatoid arthritis. II. In vivo effects on bone mineral density. Rheumatology 41:741–749
19. Dolan AL, Moniz C, Abraha H, Pitt P (2002) Does active treatment of rheumatoid arthritis limit disease-associated bone loss? Rheumatology 41:1041–1047

A three-dimensional quantitative analysis of carpal deformity in rheumatoid wrists

S. Arimitsu,
T. Murase,
J. Hashimoto,
K. Oka,
K. Sugamoto,
H. Yoshikawa,
H. Moritomo

From Osaka University Graduate School of Medicine, Osaka, Japan

We have measured the three-dimensional patterns of carpal deformity in 20 wrists in 20 rheumatoid patients in which the carpal bones were shifted ulnarwards on plain radiography. Three-dimensional bone models of the carpus and radius were created by computerised tomography with the wrist in the neutral position. The location of the centroids and rotational angle of each carpal bone relative to the radius were calculated and compared with those of ten normal wrists.

In the radiocarpal joint, the proximal row was flexed and the centroids of all carpal bones translocated in an ulnar, proximal and volar direction with loss of congruity. In the midcarpal joint, the distal row was extended and congruity generally well preserved. These findings may facilitate more positive use of radiocarpal fusion alone for the deformed rheumatoid wrist.

The most common deformity of the wrist in rheumatoid arthritis (RA) has been described as carpal supination with ulnar translocation[1] and many reports have attempted to evaluate this deformity.[2-8] However, they have been two-dimensional studies based generally on radiological assessment, the value of which is limited because the complex, overlapping appearance makes measurement difficult, especially in wrists with severe deformity. We have therefore undertaken an analysis of such deformities using a new three-dimensional (3D) technique.

Patients and Methods

We studied 20 wrists in 20 rheumatoid patients in which there was ulnar translocation on the anteroposterior radiograph. We chose wrists with a carpal-ulnar distance ratio below 0.27[9] and in which the shape of each bone was easily recognisable (Fig. 1). There were 19 women and one man with a mean age of 61 years (21 to 80). The mean duration of the disease was 15 years (6 to 38). A total of 18 patients had the more erosive subset of the disease, one the least erosive[10] and one juvenile RA. For comparison, we also chose a control group of ten normal wrists in ten men with a mean age of 41.4 years (18 to 76).

Imaging. Computerised tomography (CT) with a slice thickness of 0.625 mm was undertaken on a clinical helical-type scanner (LightSpeed Ultra16; General Electric, Maukesha, Wisconsin). During image acquisition, the wrists were in the neutral position with the axes of the third metacarpal and forearm aligned. The data were saved in a standard format (DICOM; Digital Imaging and Communications in Medicine).

Segmentation and construction of three-dimensional surface bone models. Segmentation is the extraction of individual bony regions. The anatomy or region of interest must be delineated and separated so that it can be viewed individually and 3D models reconstructed. Regions of individual bones were segmented semi-automatically using a software program for image analysis (Virtual Place-M; AZE Ltd, Tokyo, Japan). Surface models of the radius and each carpal bone were obtained by 3D surface generation of the bone cortex.[11-13]

Measurement of centroid translocation and carpal rotation. First, the position of the volume centroid of any bone was calculated from the CT files.[14] In order to measure the translocation, we defined the grid for the lower radius and each carpal bone within it. This was the orthogonal reference system originally advocated by Belsole et al[15] (Figs 2 and 3). For the radius this was determined as follows: The Y axis was the longitudinal radial axis and indicated the proximal (+)/distal (-) direction; the Z axis was the line through the styloid perpendicular to the Y axis and indicated radial (+)/ulnar (-) displacement; the X axis was the

• S. Arimitsu, MD, Orthopaedic Surgeon
• T. Murase, MD, PhD, Assistant Professor
• J. Hashimoto, MD, PhD, Associate Professor
• K. Oka, MD, Orthopaedic Surgeon
• K. Sugamoto, MD, PhD, Professor
• H. Yoshikawa, MD, PhD, Professor
• H. Moritomo, MD, PhD, Assistant Professor
Department of Orthopaedic Surgery
Osaka University Graduate School of Medicine, 2-2, Yamada-oka, Suita, Osaka 565-0871, Japan.

Correspondence should be sent to Dr S. Arimitsu; e-mail: sayu@dfb.so-net.ne.jp

doi:10.1302/0301-620X.89B4.18476 $2.00

J Bone Joint Surg [Br] 2007;89-B:490-4.
Received 31 July 2006; Accepted after revision 5 December 2006

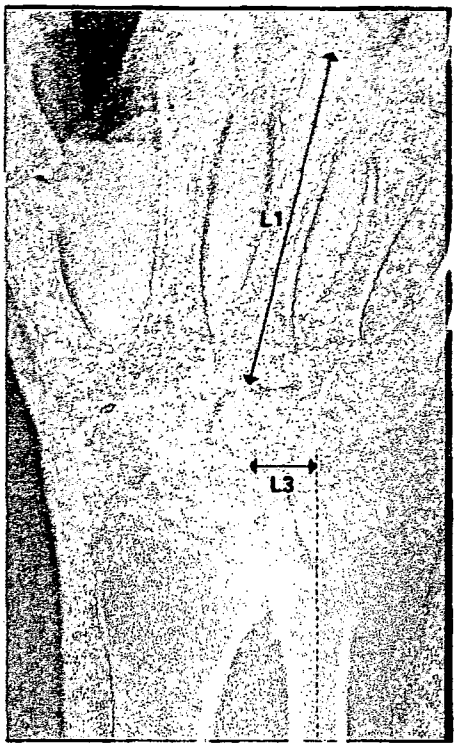

Fig. 1

Radiograph showing measurement of the carpal-ulnar distance ratio. It is calculated as L3/L1 where L3 is the distance between the centre of the capitate and the bony axis of the ulna and L1 the length of the third metacarpal. The normal ratio is 0.3 SD 0.03.

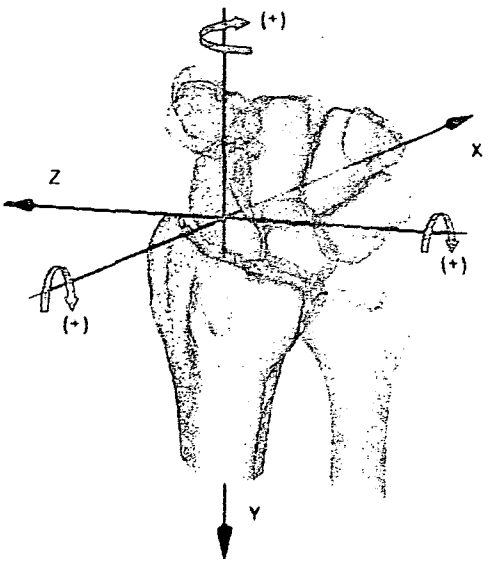

Fig. 2

A three-dimensional model showing details of the orthogonal reference system established in the radius as advocated by Belsole et al.[15] The Y axis was the longitudinal radial axis and indicated the proximal (+)/distal (-) direction; the Z axis was the line through the styloid perpendicular to the Y axis and indicated radial (+)/ulnar (-) displacement; the Y axis was the line perpendicular to the YZ plane and indicated palmar (+)/dorsal (-) displacement. Rotation around the Z axis produced flexion (+)/extension (-); that around the Y axis pronation (+)/supination (-) and that around the X axis indicated ulnar (+)/radial (-) deviation.

line perpendicular to the YZ plane and indicated palmar (+)/dorsal (-) displacement. Rotation around the Z axis produced flexion (+)/extension (-); that around the Y axis pronation (+)/supination (-) and that around the X axis indicated ulnar (+)/radial (-) deviation (Fig. 2). Thus, we calculated as a 3D vector the translocation of each carpal bone relative to the reference system determined for the radius.[13,15]

Next, using the anatomical feature as described by Belsole et al[14] the local co-ordinate system for the scaphoid, lunate, and capitate was established to characterise carpal direction (Fig. 3). The X axis of the scaphoid was defined as its principal axis, calculated as the line on which the moment of inertia was smallest and which ran through the centroid. The Z axis was defined as the line running through the dorsal ridge of the scaphoid in the plane perpendicular to the X axis and the Y axis was the line perpendicular to the XZ plane. The X axis of the lunate was defined as the line through the palmar and dorsal poles, the Y axis as the line through the centroid, perpendicular to the X axis and the Z axis as the line perpendicular to the XY plane. The Y axis of the capitate was defined as its principal axis[14] and the Z axis as the line through the dorsal joint ridge of the capitate-hamate joint perpendicular to the Y axis, rotated +90° around the Y axis. The X axis was the line perpendicular to the YZ plane. From these planes the 3D vector of a carpus relative to the radius was calculated with six degrees of freedom using the Euler angle[12] method. This quantified the direction and rotation of each carpal bone in the RA wrist relative to the radius and compared their positions with those of a normal wrist.

With regard to evaluating the translocation of location of the centroid, the variation in size of each carpal bone needed to be considered, and the translocation index was used for the purpose. It was calculated by dividing each of the three components of the vector of the centroids of the carpal bones by the square root of the cross-section of the radius at a plane perpendicular to its longitudinal axis and passing through Lister's tubercle[16] (Fig. 4).

The translocation index was as follows:

$(Tx, Ty, Tz) = x/\sqrt{S}, y/\sqrt{S}, z\sqrt{S})$,

where x, y and z represent the vectors of the centroid of the carpal bone, relative to the origin of the reference of the

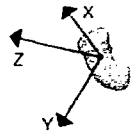

Fig. 3a

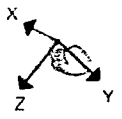

Fig. 3b

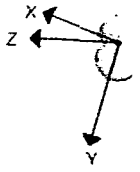

Fig. 3c

Diagram showing the orthogonal system as applied to a) the scaphoid, b) the lunate and c) the capitate according to Belsole et al.[14] The X axis of the scaphoid was defined as its principal axis, calculated as the line on which the moment of inertia was smallest and which ran through the centroid. The Z axis was defined as the line running through the dorsal ridge of the scaphoid in the plane perpendicular to the X axis, and the Y axis was the line perpendicular to the XZ plane. The X axis of the lunate was defined as the line through the palmar and dorsal poles, the Y axis as the line through the centroid, perpendicular to the X axis, and the Z axis as the line perpendicular to the XY plane. The Y axis of the capitate was defined as its principal axis and the Z axis as the line through the dorsal joint ridge of the capitate-hamate joint perpendicular to the Y axis, rotated +90° around the Y axis. The X axis was the line perpendicular to the YZ plane.

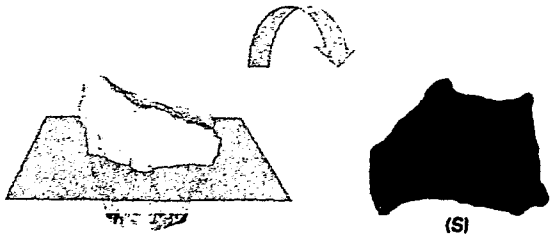

Fig. 4

Diagram showing the cross-section of the radius through Lister's tubercle, perpendicular to the longitudinal axis, S was the cross-sectional area of the radius (mm^2).

radius (mm) and S was the cross-sectional area of the radius (mm^2), at a plane perpendicular to its longitudinal axis at the level of Lister's tubercle (Fig. 4).

Statistical analysis. The left hand was converted to the orientation of the right and comparison of the results between the control and RA groups performed using standard statistical formulae based on the Mann-Whitney U-test. The results were deemed to be significant if $p \leq 0.05$.

Results

Centroid translocation. Three-dimensional images of the carpal bones showed that all centroids translocated not just in an ulnar direction, but also in the ulnar, proximal and volar direction, along the slope of the surface of the distal radius (Figs 5 and 6). Contacts between the radius and the scaphoid and the radius and the lunate were translocated ulnopalmarly and were incongruent in most cases. In the midcarpal joint, congruity was relatively well preserved compared with that of the radiocarpal joint in most cases (Fig. 7) while their radiographs showed joint narrowing (Fig. 1).

In the radioulnar deviation plane, the capitate ($p = 0.0011$) hamate, ($p = 0.0013$), lunate ($p < 0.0001$), scaphoid ($p = 0.0003$), triquetrum ($p < 0.0001$) and trapezoid ($p = 0.0197$), in RA wrists were significantly translocated to the ulnar side by a mean of 6.28, 4.68, 5.07, 7.10, 3.85 and 6.12 mm, respectively (Table I). In the flexion-extension plane all the centroids translocated in the palmar and proximal directions relative to the radius. The capitate ($p = 0.0083$), hamate ($p = 0.0037$) and scaphoid ($p = 0.0064$) in RA wrists were significantly translocated in the palmar direction by a mean of 3.21, 2.99 and 2.04 mm, respectively (Table I). The capitate ($p < 0.0001$), hamate ($p = 0.0037$), lunate ($p < 0.0001$), scaphoid ($p < 0.0001$) triquetrum ($p = 0.0011$), trapezium ($p < 0.0001$) and trapezoid ($p < 0.0001$) in RA wrists were significantly translocated proximally by a mean of 10.70, 9.41, 8.68, 6.90, 9.89, 11.37 and 13.30 mm, respectively (Table I).

Carpal rotation. The proximal row of RA wrists was flexed significantly compared with the normal wrists (Fig. 7b), the scaphoid at 25° ($p = 0.0003$) and the lunate at 10° ($p = 0.0311$) more than normal. In the pronation/supination plane, the scaphoid, lunate, and capitate did not supinate but were pronated 12°, 7° and 6°, respectively ($p = 0.053$, 0.147 and 0.356). The distal row was extended dorsally (Fig. 7c), as was the capitate by 12° ($p = 0.0387$) more than normal. The 3D images showed that the dorsally extended distal row corrected the hand to almost normal relative to the radius, by counteracting the flexion deformity of the proximal row.

Discussion

In the RA wrist, ligamentous laxity is probably the major cause of collapse and instability.[1] There are many reports which have attempted to measure the deformity radiologically,[2-4,6-8] but two-dimensional evaluation is of limited value. In our study, 3D imaging showed clearly that the rheumatoid carpus translocated obliquely in an ulnar, proximal and volar direction (Fig. 6). This quantitative technique allowed an easier understanding of this complex deformity. The direction of carpal translocation followed the natural slope of the joint surface of the distal radius which had a mean inclination of 24° in the coronal and 11° in the sagittal plane.[16,17] In normal wrists, displacement of the carpus was resisted mainly by the palmar and dorsal radiotriquetral and palmar radiolunate ligaments.[6,18,19] Their laxity probably allowed the 3D oblique translocation.

Rotational deformity, one of the most common deformities in RA, has been described qualitatively as carpal supination. Our 3D study, however, showed quantitatively that the main rotational deformity of the proximal row was